particles

MDPI

Article

Deep Learning with RESNET 18 for High-Precision Laser Crater Data Processing

Nour Jalal Abdulameer [1,2]

[1] NAPLIFE-WIGNER Institute, 1121 Budapest, Hungary; nour.abdulameer@wigner.hu or nmnm.2014829@gmail.com; Tel.: +36-20-500-1667
[2] Doctoral School of Physics, University of Debrecen, 4032 Debrecen, Hungary

Abstract

This research investigates crater formation during laser ablation of polymerized UDMA–TEGDMA composites, focusing on the quantitative analysis of crater volume and depth under varying laser intensities. Two types of samples were examined: composites without gold nanorods (Au0, reference sample) and composites containing resonant gold nanorod dipole antennas (Au2, plasmonic sample), with the nanorod dimensions tuned to the frequency of the incident laser irradiation. These resonant plasmonic targets were originally developed and investigated within the NAPLIFE (Nano-Plasmonic Laser Induced Fusion Energy) Collaboration, initiated in 2019. The incorporation of resonant gold nanorods enhanced the laser-induced ablation response, resulting in larger crater volumes and greater crater depths at higher laser pulse energies. In contrast, gold nanorods with non-resonant dimensions did not exhibit comparable enhancement, demonstrating that the observed effect is associated with the resonant geometry of the nanorod dipole antennas rather than simply with the presence of gold nanoparticles. Reference-line values were used to establish baseline comparisons, while the average crater depth served as a key indicator of material removal. Building on these experimental findings, the study further integrates artificial intelligence for automated crater analysis. A deep transfer learning approach using a fine-tuned ResNet-18 model was implemented to classify high-resolution crater images of Au0 and Au2 samples. By retraining the final fully connected layer while freezing the convolutional feature extractor, the model achieved a validation accuracy of 98.7 percent, demonstrating stable convergence. The results confirm that deep learning offers a powerful and reproducible framework for high-precision classification and analysis of laser-induced surface structures, paving the way for intelligent materials diagnostics and laser-process optimization.

Keywords: RESNET 18; deep learning; laser crater; gold nanorods; UDMA-TEGDMA composites; volume of the crater; depth of the crater; materials analysis; transfer learning; PyTorch; classification

Check for updates

Academic Editors: David Blaschke, Tamás S. Biró, Ralf Schützhold and Mª Ángeles Pérez García

Received: 26 November 2025
Revised: 13 September 2026
Accepted: 30 September 2026
Published: 8 October 2026

Copyright: © 2026 by the author. Licensee MDPI, Basel, Switzerland. This article is an open access article distributed under the terms and conditions of the Creative Commons Attribution (CC BY) license.

1. Introduction

In laser–material interactions, a high-intensity laser beam is concentrated on the surface of a material [1]. The laser energy rapidly raises the temperature and vaporizes the surface material, resulting in a localized explosion, as illustrated in Figure 1. This explosive occurrence leads to the expulsion of material from the surface, culminating in the creation of a crater at the impact site [2]. The process is influenced by several physical processes, including heat conduction, surface melting, and vaporization, followed

by recoil pressure and the ejection of evaporated material [3]. The crater's depth and size are affected by parameters such as laser pulse energy and material characteristics, including the presence of embedded particles or nanostructures that might improve ablation efficiency [4]. Comprehending this connection is essential for enhancing processes across several disciplines, such as material science and microfabrication.

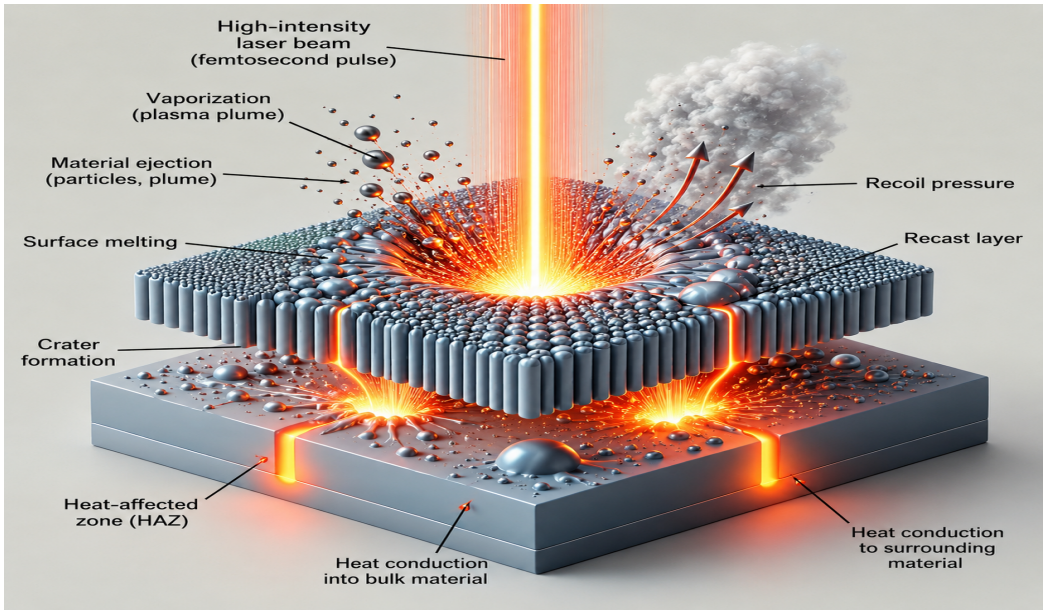

Figure 1. Schematic illustrating laser–material interaction, depicting surface melting, vaporization, and crater creation resulting from high-intensity laser irradiation, with an emphasis on heat conduction and recast layer generation.

The initial characterization experiments were performed at the HUN-REN Wigner Research Centre for Physics (NAPLIFE-WIGNER Institute), Budapest, Hungary [5–7], to characterize and compare the structural response of polymerized UDMA–TEGDMA composite samples with and without embedded gold nanorod dipole antennas. The purpose of these measurements was to investigate the spatial distribution of displacement and deformation and to provide complementary structural characterization of the composite targets. Such characterization is relevant to the NAPLIFE laser–matter interaction studies, where UDMA–TEGDMA targets with and without resonant gold nanorods were investigated to determine the influence of plasmonic nanoparticles on laser-induced crater formation and material removal [8–10].

The UDMA–TEGDMA composite targets were prepared within the NAPLIFE project following the procedure described by Bonyár et al. [7]. The Au0 target consisted of a UDMA–TEGDMA monomer mixture at a 3:1 ratio, polymerized to a thickness of approximately 400 μm. The Au2 target was prepared using the same polymer matrix with plasmonic gold nanorods fabricated by Nanopartz Inc. (USA), incorporated at a concentration of 2.8×10^{12} nanoparticles/mL. The resonant gold nanorods had dimensions of approximately 25 nm × 85 nm. For comparison, the non-resonant nanorods had dimensions of approximately 25 nm × 35 nm. The prepared Au0 and Au2 targets were subsequently used as reference and plasmonic targets, respectively, in the femtosecond laser irradiation experiments [7,10].

Below is an analysis of the principal components shown in Figure 2:

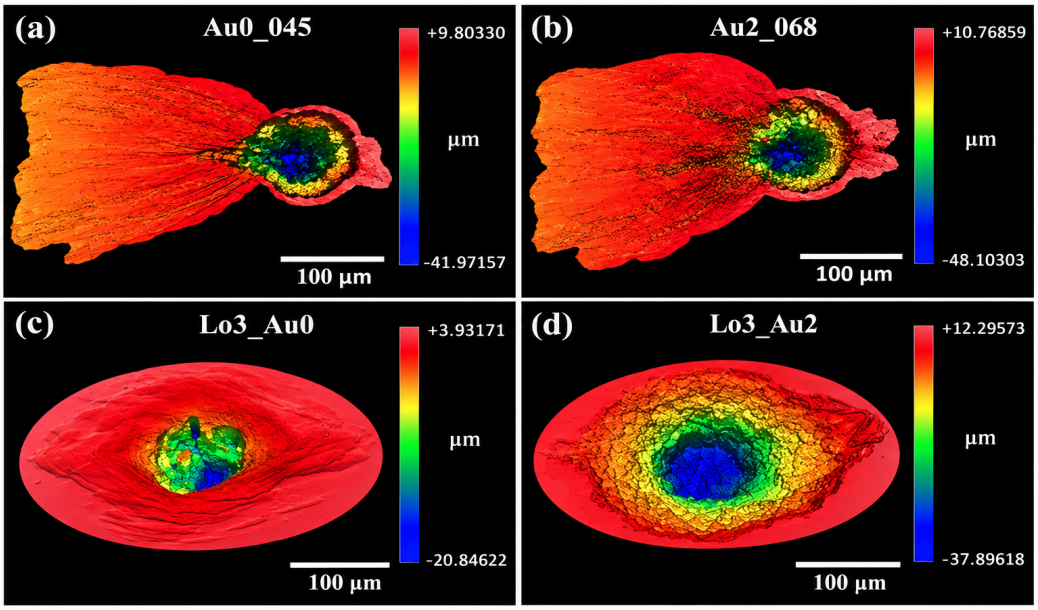

Figure 2. Deformation maps of UDMA-TEGDMA composite samples without gold nanorods (Au0) and containing gold nanorod dipole antennas (Au2). Panels (**a**–**d**) correspond to Au0_045, Au2_068, Lo3_Au0, and Lo3_Au2, respectively. The color scale represents displacement in micrometers (µm), and the scale bars correspond to 100 µm.

Types of samples:

- Au0 (Without Gold) : This denotes the UDMA-TEGDMA composite material without the inclusion of gold particles.
- Au2 (With Gold): This refers to the same polymerized composite material, but augmented with gold particles to improve certain properties, presumably mechanical or thermal.

For clarity, the nomenclature used in Figure 2 is defined as follows.

The label Au0 denotes the reference UDMA–TEGDMA composite without embedded gold nanorods, whereas Au2 denotes the UDMA–TEGDMA composite containing gold nanorods with dimensions selected to provide plasmonic resonance with the 795 nm laser wavelength [7,10]. The numerical extensions, such as 045 and 068, identify the corresponding individual records or images in the experimental dataset. "LO3" denotes a specific longitudinal optical phonon mode that tracks energy transfer from laser-excited electrons to the physical target structure. The four panels correspond to Au0_045, Au2_068, Lo3_Au0, and Lo3_Au2, respectively. The color maps represent the spatial distribution of displacement/deformation in micrometers (µm), while the scale bars correspond to 100 µm.

- In the upper left panel (Au0_045), the range is from +9.80330 µm to −41.97157 µm.
- In the bottom right panel (Lo3_Au2), the range is from +12.29573 µm to −37.89618 µm.

Volume Assessment:

The text at the bottom suggests the need to determine the volume of these different materials or structures. This likely involves using the deformation data to compute the three-dimensional volume changes or the total volume based on the displacement distribution across the composite samples.

The UDMA–TEGDMA composite was selected as the target material because it provides a suitable polymer matrix for incorporating plasmonic gold nanorod dipole antennas and for investigating their influence on laser–matter interaction. In the NAPLIFE approach, the gold nanorods were selected with dimensions corresponding to plasmonic resonance

with the wavelength of the incident femtosecond laser, enabling enhanced interaction between the laser field and the embedded nanostructures [5–7,10]. The UDMA–TEGDMA system therefore provides a controlled material platform for comparing reference targets without gold nanorods (Au0) with plasmonic targets containing resonant gold nanorods (Au2), particularly with respect to laser-induced ablation and crater formation [7,10].

While the analysis focuses on the physical and mechanical behavior of laser-induced craters in UDMA–TEGDMA composites, understanding and classifying crater morphologies across large datasets remains a significant challenge. Traditional manual inspection is both time-consuming and prone to subjective bias. To address this limitation and to further enhance the precision of crater analysis, the present study introduces a computational approach based on deep learning. In this continuation of the work shown in Figure 3 the RESNET 18 architecture, is employed to automatically identify and classify crater patterns formed under different material and laser conditions.

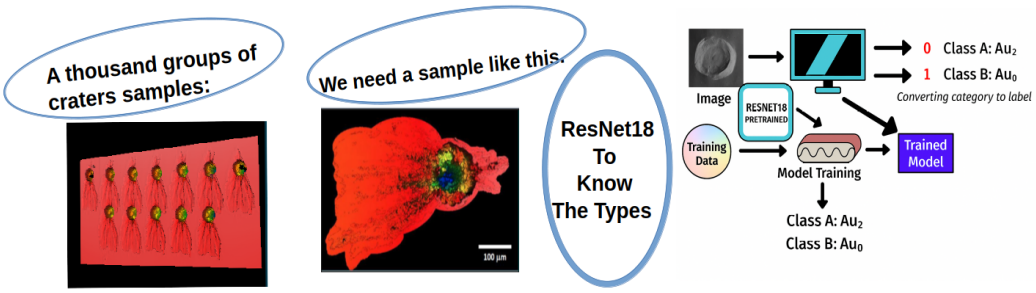

Figure 3. Workflow of the deep learning crater classification pipeline. Image data (Au0 and Au2) were preprocessed, augmented, and fed into a fine-tuned RESNET 18 model for binary classification.

In recent years, artificial intelligence (AI) and deep learning have become powerful analytical tools in materials science, particularly for image-based feature detection, classification, and pattern recognition. Deep learning models—especially convolutional neural networks (CNNs)—are inspired by biological vision systems and consist of multiple processing layers that learn hierarchical representations of image data [11]. CNNs automatically extract features from raw images, such as edges, textures, and complex spatial structures, making them ideal for analyzing laser crater morphologies where subtle surface variations must be identified and classified.

A major limitation of conventional deep neural networks is the vanishing gradient problem, which restricts their depth and learning efficiency. The introduction of the Residual Network (ResNet) architecture by He et al. (2016) revolutionized this field by incorporating skip or identity connections that allow gradients to flow more effectively during backpropagation [12]. Each residual block in ResNet learns a residual mapping of the input rather than the complete transformation, effectively stabilizing the training of very deep models.

The RESNET 18 architecture, containing 18 trainable layers, represents one of the most computationally efficient variants within the ResNet family. It is composed of multiple convolutional and batch normalization layers interleaved with nonlinear activation functions (ReLU), followed by residual connections that preserve feature integrity. This design not only reduces training time but also improves the model's ability to generalize to new datasets. Compared with deeper models like ResNet50 or ResNet101, RESNET 18 provides a favorable trade-off between computational cost and accuracy, which is particularly advantageous for medium-sized experimental datasets such as crater images obtained from laser ablation studies.

In this work, the RESNET 18 network was utilized through transfer learning to classify crater images corresponding to UDMA–TEGDMA composites with and without gold

nanorods (Au0 and Au2). Transfer learning leverages pre-trained weights from large-scale datasets, such as ImageNet, to capture low-level image features that can then be fine-tuned for specialized applications [13]. Only the final fully connected layer of the RESNET 18 model was retrained, while the convolutional layers were frozen to retain generalized visual representations. This approach minimizes computational effort and reduces the risk of overfitting while achieving high classification accuracy with a limited dataset.

Applying RESNET 18 to crater image analysis enables automated and reproducible classification of laser-ablated surfaces, reducing the subjectivity associated with manual assessment. The model learns morphological differences in crater structures associated with the presence or absence of gold nanorods, which are related to changes in heat absorption, ablation efficiency, and surface modification. Identifying these morphological changes is important because crater geometry and surface characteristics provide indirect information about the interaction between the laser radiation and the composite material. In particular, differences in crater formation can be used to evaluate how the incorporation of gold nanorods influences laser energy deposition and material removal. This information is valuable for optimizing laser processing conditions and for designing composite materials with controlled surface characteristics for specific applications. Thus, the integration of physics-driven experimentation with data-driven modeling provides a robust framework for automated materials characterization, high-precision diagnostics, and process optimization.

2. Experimental Setup

A high-intensity laser beam was focused onto the surface of the polymerized UDMA–TEGDMA composites. Two sets of samples were prepared: Au0 (without gold nanoparticles) and Au2 (with gold nanoparticles). In the Au2 samples, the incorporated gold nanoparticles were in the form of gold nanorods, which act as resonant dipole nanoantennas under optical excitation. Their localized surface plasmon resonance enhances the absorption of laser radiation and promotes localized energy deposition and conversion into heat within the surrounding polymer matrix. This optical response is essential for understanding the effect of gold nanorods on the material's response to laser irradiation. A range of laser intensities was applied to evaluate how the presence of gold nanorods influences the structural response of the material. Crater dimensions and surface deformations were recorded using a high-speed camera and surface profilometry [14].

The experimental setup for the laser crater experiment is depicted in Figure 4 [15]. A Ti:Sapphire laser with a wavelength of 795 nm and a pulse length of 42 fs was employed, operating at an intensity range of 10^{16}–10^{17} W/cm^2 and a pulse energy of 1 to 25 mJ. The laser beam (LB) was directed onto the target (T) using a combination of mirrors (M) and lenses (L).

The key components of the setup include:

- VAC: Vacuum chamber to control the environment, with a pressure of 10^{-6} Pa.
- HSM and HSC: High-speed monochrome and color cameras were used, respectively, to capture real-time images of crater formation.
- BPC: Beam profiling camera, used to monitor and maintain laser beam uniformity.
- P and DM: Periscope and dropping mechanism for precise laser alignment and control of the laser-target interaction.
- LED and HAL: LED and halogen lamps for additional illumination during the experiment.
- TSC: PTFE screen to protect components from the laser beam.
- HM: Holding magnet, used to secure the target (T) in place during the experiment.

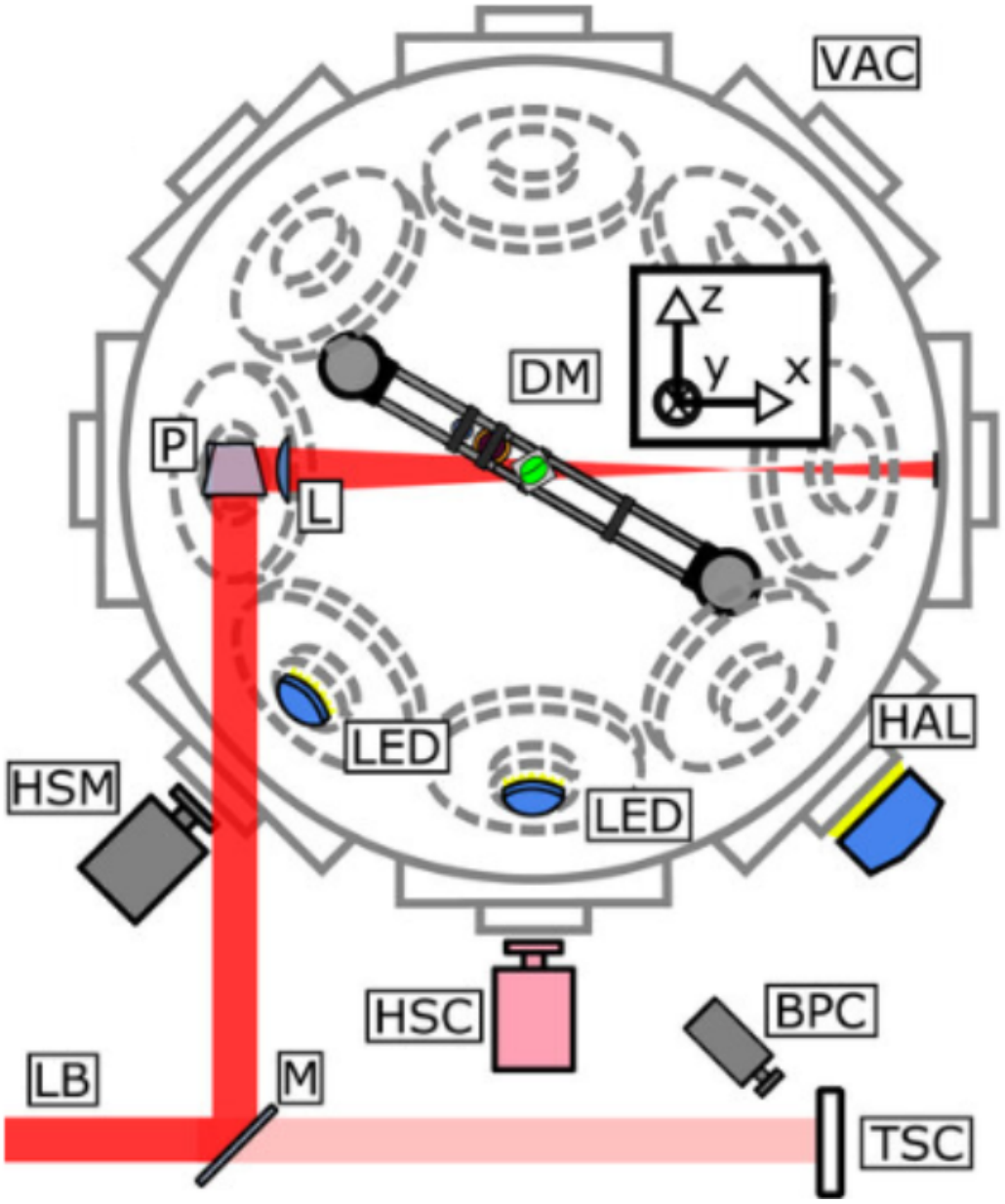

Figure 4. Schematic representation of the experimental setup for the laser crater experiment.

The experiment was carried out at an illumination angle of 45°, and the burn pattern was recorded using a burn pattern foil (BP). The Au nanorods were homogeneously dispersed within the UDMA–TEGDMA polymer matrix by ultrasonic stirring; therefore, no preferential orientation of the nanorods with respect to the laser propagation direction or polarization was imposed. The nanorods were designed to exhibit plasmonic absorption resonant with the 795 nm wavelength of the femtosecond laser. Consequently, the laser interaction occurred with nanorods having different orientations relative to the incident electric field. The Au2 sample contained gold nanorods at a concentration of 2.8×10^{12} nanoparticles/mL. The resonant nanorods had dimensions of approximately 25 nm × 85 nm.

The laser pulse energies were varied across several trials (1, 5, 10, 15, 20, and 25 mJ), and the resulting crater dimensions were analyzed in terms of depth and volume.

3. Collection and Processing of Raw Data

The data collection process focused on obtaining surface profile measurements for both types of samples: with gold (Au2) and without gold (Au0). The procedures outlined

below ensured consistent processing of the measured profiles and provided information on the morphological characteristics of the laser-induced craters.

The flow of the data collection and analysis process is illustrated by the following steps:

1. Crater Raw Data Collection: Surface profile data were collected for the Au2 (with gold nanorods) and Au0 (without gold nanorods) samples. The measured surface profile consists of the surface height (or depth) z as a function of the lateral measurement position.
2. Smoothing: A moving-average smoothing algorithm was applied to reduce measurement noise while preserving the main characteristics of the crater profile. The smoothed surface profile, $z_{\text{smooth}}(i)$, was calculated as:

$$z_{\text{smooth}}(i) = \frac{1}{n}\sum_{j=1}^{n} z(j),$$

where $z(j)$ represents the measured surface height (or depth) at the j-th data point within the smoothing window, i denotes the position of the smoothed data point, and n is the number of data points included in the smoothing window. In this analysis, a window size of $n = 17$ data points was selected to effectively reduce high-frequency measurement noise while minimizing distortion of the actual crater profile.

The smoothed data were compared with the corresponding raw data for each sample. As shown in Figure 5, the smoothing process effectively reduced noise and provided clearer representations of the crater profiles.

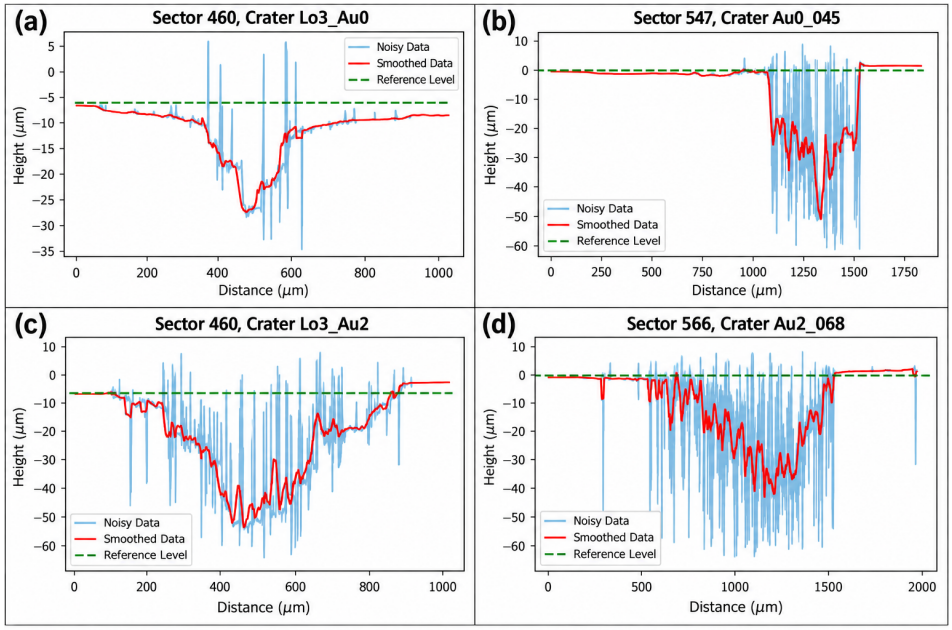

Figure 5. Data smoothing using a moving-average method for different crater measurement sectors and samples, including Sector 460 (Crater L03_Au0 and Crater L03_Au2), Sector 547 (Crater Au0_045), and Sector 566 (Crater Au2_068). Here, a *sector* refers to a selected region of the measured surface-profile data corresponding to a specific crater area. The sector numbers (460, 547, and 566) are the identifiers assigned to these measurement regions in the surface-profile dataset.

3. Volume Calculation: Two methods were employed to calculate the volume of material removed:
   - Trapezoidal Rule: The trapezoidal rule was used to numerically integrate the measured crater profile and estimate the corresponding cross-sectional area,

which was subsequently used in the volume calculation. For equally spaced measurement points, the numerical integral is given by:

$$\int_a^b f(x)\,dx \approx \frac{h}{2}\left[f(a) + 2\sum_{i=1}^{n-1} f(x_i) + f(b)\right],$$

where a and b are the lower and upper limits of integration, respectively; $f(x)$ is the measured crater-profile function, with $f(x_i)$ representing the profile value at the i-th measurement point; h is the uniform spacing between consecutive measurement points; x is the spatial coordinate along the measured crater profile; x_i is the spatial coordinate of the i-th measurement point; i is the index of the measurement points; and n is the total number of measurement points included in the integration.

As shown in Figure 6, the volume calculations for different craters varied:

- Sector 320, Crater L03_Au0: The calculation was unable to be made due to irregularities in the crater profile.
- Sector 367, Crater L03_Au2: The volume was calculated as 28 µm^3, showing a well-defined crater.
- Sector 625, Crater Au0_045: The volume was estimated at 35 µm^3, with a deeper crater profile.
- Sector 631, Crater Au2_068: The volume was 30 µm^3, indicating clear material displacement.

The trapezoidal rule provided initial volume estimates, with more consistent results for gold-containing samples (Au2), suggesting improved material removal properties due to the presence of gold.

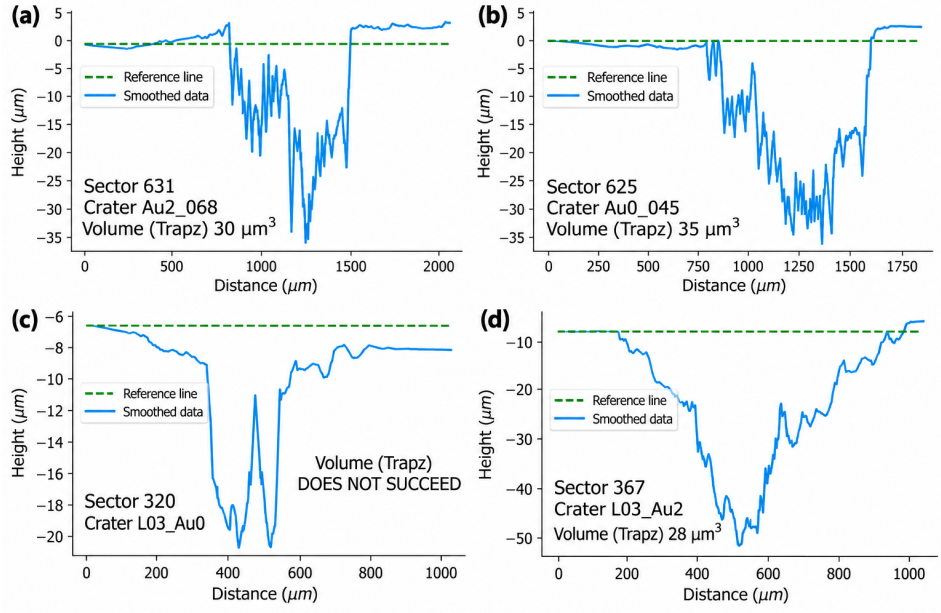

Figure 6. Volume calculation results using the trapezoidal rule for different sectors and craters: (**a**) Sector 320, crater L03_Au0; (**b**) Sector 625, crater Au0_045; (**c**) Sector 367, crater L03_Au2; and (**d**) Sector 631, crater Au2_068. The blue curves represent the smoothed crater profiles, while the green dashed lines indicate the reference surfaces used for the volume calculations.

- Simpson's Rule: Simpson's rule was also applied to numerically integrate the measured crater profile. For equally spaced measurement points and an even number of intervals, the numerical integral is given by:

$$\int_a^b f(x)\,dx \approx \frac{h}{3}\left[f(a) + 4\sum_{\substack{i=1\\ i\ \text{odd}}}^{n-1} f(x_i) + 2\sum_{\substack{i=2\\ i\ \text{even}}}^{n-2} f(x_i) + f(b)\right],$$

where a and b are the lower and upper limits of integration, respectively; $f(x)$ is the measured crater-profile function; x is the spatial coordinate along the measured crater profile; x_i is the spatial coordinate of the i-th measurement point; h is the uniform spacing between consecutive measurement points; i is the index of the measurement point; and n is the total number of measurement points included in the integration. The terms multiplied by 4 correspond to the interior measurement points with odd indices, while the terms multiplied by 2 correspond to the interior measurement points with even indices. The first and last profile values, $f(a)$ and $f(b)$, are included with a coefficient of 1.

As shown in Figure 7, the volume calculations using Simpson's rule were obtained from the numerically integrated crater-profile data.

- Sector 320, Crater L03_Au0: The volume calculation using Simpson's rule did not succeed due to irregularities in the crater profile.
- Sector 367, Crater L03_Au2: The volume was calculated as 29 µm^3, indicating a well-defined crater with a regular profile.
- Sector 625, Crater Au0_045: The volume was estimated at 35.7 µm^3, showing a deeper crater and a more regular profile compared to the previous calculation using the trapezoidal rule.
- Sector 631, Crater Au2_068: The volume was calculated as 30.445 µm^3, indicating that Simpson's rule provided a more accurate estimate of material removal compared to the trapezoidal rule.

Simpson's rule is particularly beneficial for calculating the volume in cases where the crater surface is irregular or where the profile data is highly variable. This method provides a more accurate estimate than the trapezoidal rule by using parabolic approximations. The gold-containing samples (Au2) consistently showed more regular and well-defined crater profiles, which led to more reliable volume calculations.

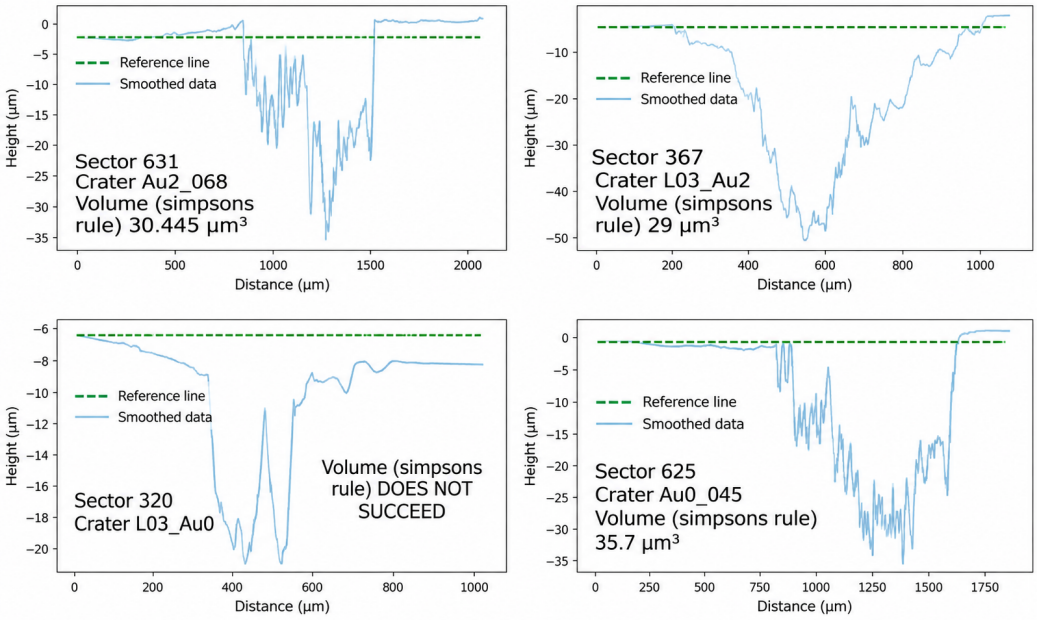

Figure 7. Volume calculation using Simpson's rule for different crater sectors and samples.

4. Reference Line for Volume: A reference line, as shown in Figure 8, was established to represent the estimated original, undisturbed surface of the polymer surrounding the crater. This reference line was used to determine the baseline surface and the maximum crater depth (z_{max}) according to:

$$z_{max} = \max(z_{ref} - z)$$

where (z_ref) represents the surface height of the established reference line (i.e., the estimated original surface level), and (z) represents the measured surface height at each point along the crater profile. The maximum value of (z_ref-z) therefore corresponds to the maximum depth of the crater relative to the reference surface.

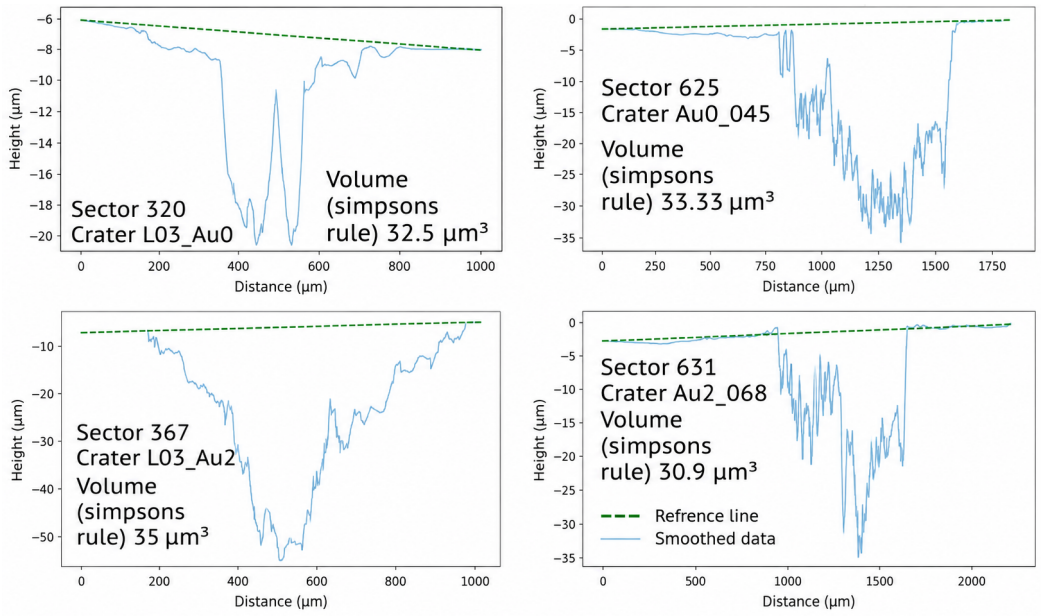

Figure 8. To define the crater's boundary, a continuous reference line is constructed to approximate the crater's surface, with the area between this smoothed curve and the reference line used to estimate the crater's volume.

5. Comparison: Finally, the results of both volume calculations were compared between the two types of sample (Au0 and Au2) to evaluate the effect of gold on surface deformation as in Figure 9.
6. Depth Comparison: Depth measurements were taken from the surface to the deepest point of the craters. The samples with gold (Au2) exhibited a higher average depth compared to those without gold (Au0), suggesting that gold enhances the removal of material under laser stress (see Table 1) & Figure 10.

Table 1. The values for each parameter are provided for different samples (Au0_045, Au2_068, L03_Au0, L03_Au2). The comparison of volume calculations using different methods (Trapz and Simpson), along with additional data for the reference line and average depth.

Parameter	Au0_045	Au2_068	L03_Au0	L03_Au2
Trapz Volume (µm^3)	239,298.4	140,376.8	4967.3	51,727.1
Simpson Volume (µm^3)	239,939.3	140,390.1	4969.8	51,729.8
Reference Line (µm^3)	399,798.2	204,668.1	7747.3	66,692.3
Average Depth (µm)	19.8	35.0	14.4	40.2

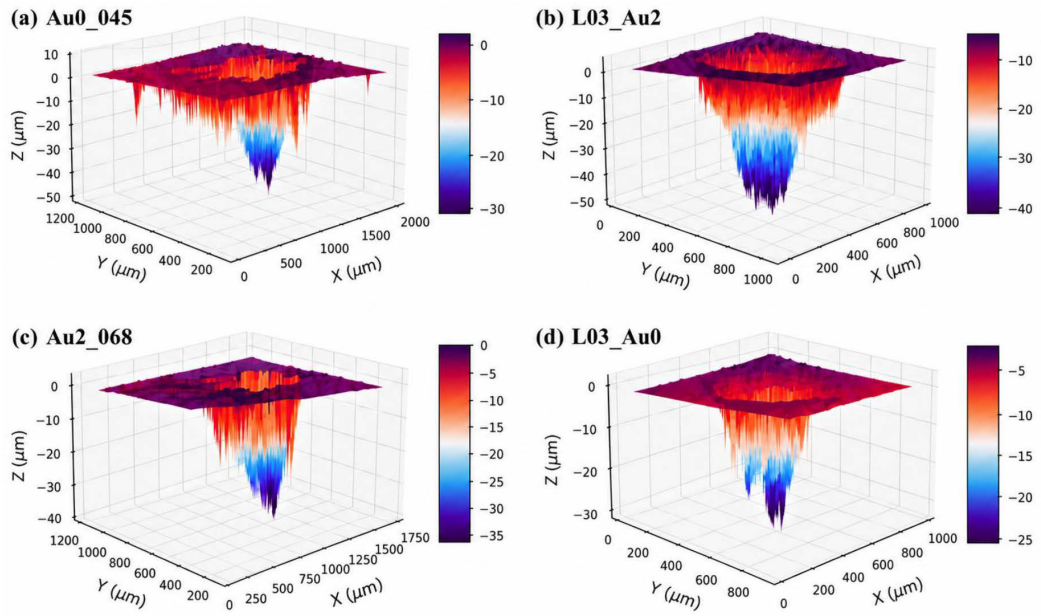

Figure 9. 3D surface plots showing crater depth and surface impact for various samples: Au0_045, L03_Au2, Au2_068, and L03_Au0. The color scale indicates depth, with darker shades representing deeper areas of the crater.

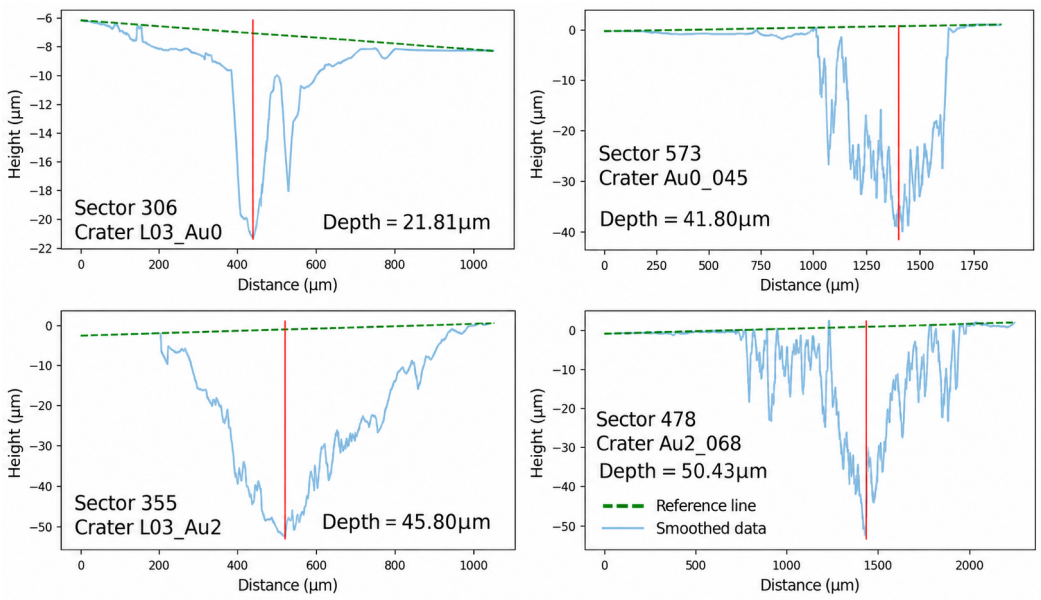

Figure 10. Depth is measured from the surface to the deepest point of the crater, highlighting the total surface impact (with gold) and focusing on damage to the underlying material (without gold).

The calculated crater volumes obtained using the trapezoidal and Simpson integration methods are presented in Table 1. The negative values in the pictures do not indicate physically negative volumes. Rather, they arise from the sign convention of the surface coordinates relative to the established reference line. Since the crater surface lies below the reference level, the numerical integration can produce a negative signed volume. The magnitude of this quantity represents the physical volume of material removed from the crater. The reference-line values similarly represent signed integrated values associated with the selected baseline and are used in determining the crater volume.

Each of these procedures guaranteed precise surface profile measurements and analysis, allowing for a thorough understanding of the properties of the composite material.

The combination of smoothing techniques and volume calculations provided accurate estimates of material removal, which is crucial to assessing the mechanical integrity of the samples.

4. Results and Discussion of Crater Properties

This section presents the experimental results of crater formation in polymerized UDMA–TEGDMA composites irradiated by a femtosecond laser. The analysis focuses on the influence of gold nanorods on crater deformation, volume, and depth, using surface profiling data and numerical integration methods.

Figure 2 shows the spatial distribution of surface displacement, expressed in micrometers (µm), for both the Au0 (without gold nanorods) and Au2 (with gold nanorods) samples. Here, displacement refers to the difference in the measured surface position relative to the established reference (undisturbed) surface level. Thus, the displacement represents the local change in surface height produced by laser irradiation, with positive and negative values indicating displacement in opposite directions according to the adopted coordinate convention. The color maps illustrate the spatial variation of the measured surface displacement across the crater area.

The Au2 samples exhibit a larger maximum surface displacement, reaching +12.29573 µm, compared with +9.80330 µm for Au0. This difference indicates that the presence of gold nanorods is associated with a greater modification of the local crater surface during laser irradiation. The enhanced surface displacement is consistent with the increased laser-energy absorption associated with the plasmonic response of the gold nanorods, which can promote stronger localized energy deposition and consequently greater material removal and surface modification.

Crater volumes were evaluated using both the trapezoidal and Simpson's numerical integration rules. Table 1 summarizes the calculated results. The Au2 samples consistently showed larger crater volumes and depths than Au0, reflecting greater ablation efficiency due to improved energy coupling. The enhanced absorption cross-section of gold facilitates localized plasma generation, resulting in deeper and smoother crater morphologies. The use of a reference line as a baseline was essential for accurately defining crater boundaries and estimating the true volume of material removed.

To improve measurement precision, smoothing algorithms were applied to the raw surface profile data. This reduced experimental noise and provided a clearer representation of crater geometry, enabling more accurate integration. The results obtained with Simpson's rule were slightly more precise than those from the trapezoidal method, especially in cases of irregular crater profiles.

The main findings of the crater property study are summarized as follows:

- Samples embedded with gold nanorods (Au2) exhibited higher deformation and deeper craters than those without gold (Au0).
- Crater volume and depth increased significantly with laser pulse energy, confirming a nonlinear dependence on laser intensity.
- The reference line method provided a reliable baseline for evaluating crater boundaries and background volume.
- Smoothing and numerical integration improved the accuracy and reproducibility of volume calculations.
- The presence of gold nanoparticles enhanced energy absorption, heat transfer, and plasma formation during ablation.

These results demonstrate that gold nanorods play a crucial role in amplifying laser-induced ablation by improving local thermal and optical properties of the composite.

The observed morphological and volumetric variations establish a solid experimental foundation for further computational analysis.

5. Deep Learning with RESNET 18

After conducting a detailed investigation of the physical properties, volume, and depth characteristics of laser-induced craters, the second part of this research focuses on extending the analysis using artificial intelligence. In this stage, a deep learning approach based on the RESNET 18 is employed to automatically classify crater images and distinguish between polymer samples with (Au2) and without (Au0) gold nanorods. This computational analysis complements the experimental results and enables a faster, objective, and reproducible interpretation of crater morphology.

The dataset consisted of high-resolution grayscale images of craters formed during the laser ablation experiments described earlier. Each image was labeled according to its material type (Au0 or Au2). A custom Python script automatically:

- Filtered valid image files (non-empty, in `.png` format),
- Randomly shuffled all samples to avoid ordering bias,
- Split the dataset into 80% training and 20% validation subsets.

As all images were resized and normalized prior to being loaded into PyTorch (version 2.2.1) tensors tensors. Figure 3 summarizes the workflow implemented for crater image classification.

6. Model Building & Training

A pre-trained RESNET 18 network was employed from the `torchvision.models` library. All convolutional layers were frozen to preserve generic feature extraction capability, while the final fully connected layer was replaced by a binary classifier. The model was trained for 10 epochs using the Adam optimizer (`lr` = 0.001), with a batch size of 32.

- Loss function: CrossEntropyLoss. The cross-entropy loss was used to quantify the difference between the probability distribution predicted by the RESNET 18 model and the true class distribution. For the binary classification task, the two classes correspond to Au0 (without gold nanorods) and Au2 (with gold nanorods). For a sample with true class y, the cross-entropy loss can be expressed as $\mathcal{L} = -\sum_{c=1}^{C} y_c \log(p_c)$, where C is the number of classes, y_c is the true label for class c, and p_c is the probability predicted by the model for class c. In this study, $C = 2$. Because the true label is one-hot encoded, the loss is determined primarily by the predicted probability assigned to the correct class. A high probability assigned to the correct class results in a low loss, whereas assigning a low probability to the correct class produces a higher loss. The term "entropy" originates from information theory and describes the uncertainty associated with a probability distribution. Cross-entropy therefore provides a measure of how well the predicted probability distribution agrees with the actual class labels, and minimizing this loss guides the network toward more accurate classification.
- Optimizer: Adam
- Hardware: NVIDIA GPU acceleration (CUDA)
- Evaluation metric: Validation accuracy per epoch

Training convergence was monitored via loss and accuracy curves as shown in Figure 11. The model achieved stable learning behavior with minimal overfitting.

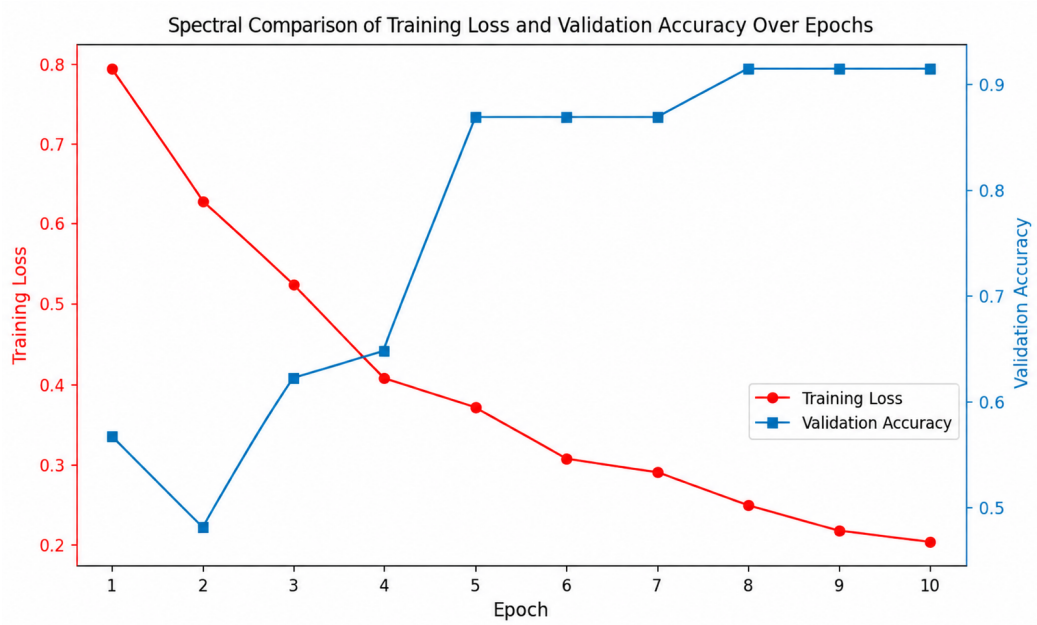

Figure 11. Training loss (red) and validation accuracy (blue) versus epochs for RESNET 18 model fine-tuned on crater dataset. The network converges smoothly to a validation accuracy of 98.7%.

Effect of Laser Intensity on ResNet18 Classification

A potential source of confusion in the classification is the dependence of crater morphology on laser pulse energy. Increasing the laser pulse energy can modify crater depth, volume, and surface morphology, and therefore a crater produced in the Au0 material at a higher pulse energy may exhibit morphological characteristics that partially overlap with those of an Au2 crater produced at a lower pulse energy. This effect was considered when interpreting the classification results.

In the present study, the ResNet18 model was trained using crater images obtained under the range of laser pulse energies investigated experimentally, rather than under a single fixed laser condition. Consequently, the image dataset includes morphological variations associated with changes in laser pulse energy as well as differences between the Au0 and Au2 materials. The classifier therefore does not rely exclusively on crater size or depth, but on the combination of spatial, textural, and morphological features present in the crater images.

The classification result should consequently be interpreted as the ability of ResNet18 to distinguish Au0 and Au2 crater morphologies within the range of laser conditions represented in the dataset, rather than as a completely intensity-independent detection of gold nanorods. The experimentally measured crater depth and volume provide complementary physical information about the influence of laser pulse energy and the presence of resonant gold nanorods. Together, these results support the use of image-based classification for identifying morphological differences between the two material types under the investigated laser conditions.

7. ResNet18 Results & Discussion

The fine-tuned ResNet18 model achieved a high validation accuracy of 98.7% in distinguishing between Au0 and Au2 crater images. This performance demonstrates that transfer learning using a moderately deep convolutional network can effectively classify subtle morphological variations in laser-induced crater patterns.

Figure 12 presents the distribution of the two image classes, confirming that the dataset was well-balanced and suitable for unbiased model training. Representative classification

outputs are displayed in Figure 13, illustrating the ability of the network to differentiate between crater morphologies corresponding to Au0 (without gold nanorods) and Au2 (with gold nanorods) samples.

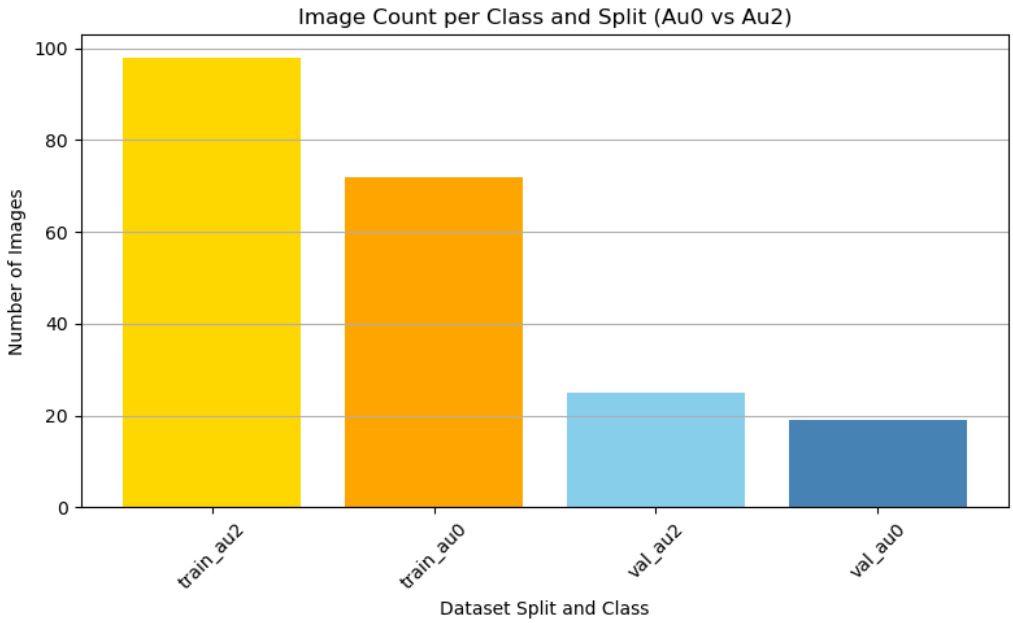

Figure 12. Class distribution of crater images for Au0 (without gold nanorods) and Au2 (with gold nanorods), demonstrating a balanced dataset that ensures unbiased learning and model convergence.

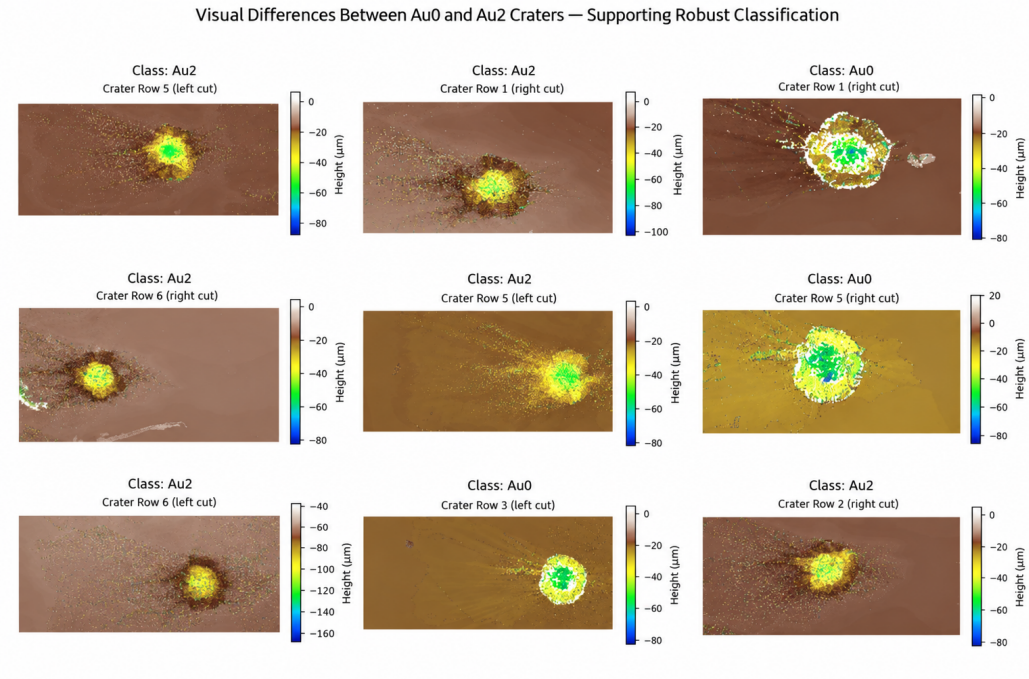

Figure 13. Representative classification results from the ResNet18 model: Au0 crater without gold nanorods; Au2 crater with gold nanorods. The model accurately identifies morphological differences induced by material composition.

The high classification accuracy achieved by ResNet18 indicates that even a relatively shallow convolutional architecture can capture the essential geometric and textural features distinguishing the two material types. This confirms that crater morphology contains sufficient discriminative information for AI-based analysis and that deep learning can complement experimental crater property measurements such as volume and depth.

By correlating the AI classification outcomes with experimental data, it becomes possible to establish a comprehensive framework that links physical crater properties with automated image-based recognition. This integration enables faster, objective, and reproducible evaluation of laser–material interactions.

Future improvements to this approach could include:

- Implementing deeper architectures (e.g., ResNet50 or EfficientNet) for enhanced feature extraction and generalization.
- Applying Grad-CAM or attention-based visualization to identify the crater regions that most influence classification outcomes.
- Integrating the trained model into a real-time diagnostic pipeline for automated material characterization and process optimization during laser ablation experiments.

Overall, the combination of high-precision laser crater analysis and deep learning-based image classification demonstrates the potential for advanced, automated evaluation techniques in materials science and photonics research.

Conclusions of the RESNET 18

The integration of deep learning into laser–material interaction studies provides a new analytical dimension that bridges experimental measurements and computational intelligence. The experimental crater analysis presented earlier demonstrated clear differences between the Au0 and Au2 samples in terms of crater depth, volume, and surface morphology. In particular, the incorporation of plasmonic gold nanorods resulted in deeper craters at higher laser intensities and produced distinct surface morphologies compared with the undoped polymer. These observations demonstrate that the presence of resonant gold nanorods significantly influences the laser-induced response of the UDMA–TEGDMA composite [7,10].

The crater-depth and volume measurements therefore provided quantitative evidence of the different laser–material interaction regimes in the Au0 and Au2 samples. The observed increase in crater depth and the enhanced crater volume at higher laser intensities indicate stronger localized energy deposition in the nanorod-containing material. These experimentally measured differences provided the physical basis for applying image-based classification using RESNET 18.

The RESNET 18-based model successfully learned the morphological differences visible in the crater images and achieved near-perfect classification accuracy. Thus, the deep-learning analysis complements the conventional quantitative measurements by providing an automated and reproducible method for distinguishing crater morphologies associated with the presence or absence of gold nanorods. The combination of experimentally determined crater depth and volume with CNN-based image classification establishes a comprehensive workflow for automated materials characterization and may provide a basis for future laser-diagnostics and process-optimization systems.

Funding: This work is supported in part by the Hungarian Research Network, Laser Fusion Research Laboratory under project Nos. NKFIH-874-2/2020, NKFIH-468-3/2021, and 2022-2.1.1-NL-2022-00002.

Data Availability Statement: Data is available upon reasonable request by contacting the corresponding author.

Acknowledgments: This research was supported by the Nanoplasmonic Laser Fusion Research Laboratory and the National Research and Innovation Office of Hungary.

Conflicts of Interest: The author declares no conflicts of interest.

References

1. Chichkov, B.N.; Momma, C.; Nolte, S.; von Alvensleben, F.; Tünnermann, A. Femtosecond, picosecond and nanosecond laser ablation of solids. *Appl. Phys. A* **1996**, *63*, 109–115. [CrossRef]
2. Bäuerle, D. *Laser Processing and Chemistry*, 4th ed.; Springer: Berlin, Germany, 2011.
3. Fabbro, R.; Peyre, P.; Berthe, L.; Scherpereel, X. Physics and applications of laser-shock processing. *J. Laser Appl.* **1998**, *10*, 265–279. [CrossRef]
4. Cheng, J.; Liu, C.; Shang, S.; Liu, D.; Perrie, W.; Dearden, G.; Watkins, K.G. A review of ultrafast laser materials micromachining. *Opt. Laser Technol.* **2013**, *46*, 88–102. [CrossRef]
5. Papp, I.; Bravina, L.; Csete, M.; Kumari, A.; Mishustin, I.N.; Motornenko, A.; Rácz, P.; Satarov, L.M.; Stöcker, H.; Strottman, D.D.; et al. Kinetic model of resonant nanoantennas in polymer for laser induced fusion. *Front. Phys.* **2023**, *11*, 1116023. [CrossRef]
6. Kroó, N.; Csernai, L.P.; Papp, I.; Kedves, M.A.; Aladi, M.; Bonyár, A.; Szalóki, M.; Osvay, K.; Varmazyar, P.; Biró, T.S. Indication of p + ^{11}B reaction in Laser Induced Nanofusion experiment. *Sci. Rep.* **2024**, *14*, 30087. [CrossRef] [PubMed]
7. Bonyár, A.; Szalóki, M.; Borók, A.; Rigó, I.; Kámán, J.; Zangana, S.; Veres, M.; Rácz, P.; Aladi, M.; Kedves, M.Á.; et al. The Effect of Femtosecond Laser Irradiation and Plasmon Field on the Degree of Conversion of a UDMA-TEGDMA Copolymer Nanocomposite Doped with Gold Nanorods. *Int. J. Mol. Sci.* **2022**, *23*, 13575. [CrossRef] [PubMed]
8. Nagyné Szokol, Á; Kámán, J.; Holomb, R.; Aladi, M.; Kedves, M.; Ráczkevi, B.; Rácz, P.; Bonyár, A.; Borók, A.; Zangana, S.; et al. Pulsed laser intensity dependence of crater formation and light reflection in the UDMA-TEGDMA copolymer nanocomposite, doped with resonant plasmonic gold nanorods. *arXiv* **2024**, arXiv:2402.18138.
9. Kedves, M.; Aladi, M. High-intensity femtosecond laser irradiation experiments on polymer targets doped with gold nanorods. *Eur. Phys. J. Spec. Top.* **2025**, *234*, 3015–3019. [CrossRef]
10. Nagyné Szokol, A.; Kámán, J.; Holomb, R.; Rigó, I.; Aladi, M.; Kedves, M.; Ráczkevi, B.; Rácz, R.; Bonyár, A.; Borók, A.; et al. Morphology studies on craters created by femtosecond laser irradiation in UDMA polymer targets embedded with plasmonic gold nanorods. *Eur. Phys. J. Spec. Top.* **2025**, *234*, 3007–3013. [CrossRef]
11. Goodfellow, I.; Bengio, Y.; Courville, A. *Deep Learning*; MIT Press: Cambridge, MA, USA, 2016.
12. He, K.; Zhang, X.; Ren, S.; Sun, J. Deep residual learning for image recognition. In Proceedings of the IEEE Conference on Computer Vision and Pattern Recognition (CVPR), Las Vegas, NV, USA, 27–30 June 2016; pp. 770–778.
13. Pan, S.J.; Yang, Q. A survey on transfer learning. *IEEE Trans. Knowl. Data Eng.* **2010**, *22*, 1345–1359. [CrossRef]
14. Ivanov, D.S.; Zhigilei, L.V. Combined atomistic and continuum modeling of short-pulse laser melting and disintegration of metal films. *Phys. Rev. B* **2003**, *68*, 064114. [CrossRef]
15. Poprawe, R. *Tailored Light 2: Laser Applications Based on Shaped Pulses*; Wiley-VCH: Weinheim, Germany, 2011.

Disclaimer/Publisher's Note: The statements, opinions and data contained in all publications are solely those of the individual author(s) and contributor(s) and not of MDPI and/or the editor(s). MDPI and/or the editor(s) disclaim responsibility for any injury to people or property resulting from any ideas, methods, instructions or products referred to in the content.